

Simplicity of confinement in SU(3) Yang-Mills theory

Xavier Crean  ^{1,*} Jeffrey Giansiracusa  ^{2,†} and Biagio Lucini  ^{3,‡}

¹*Department of Mathematics, Faculty of Science and Engineering,
Swansea University, Fabian Way, Swansea, SA1 8EN, UK*

²*Department of Mathematical Sciences, Durham University,
Upper Mountjoy Campus, Durham, DH1 3LE, UK*

³*School of Mathematical Sciences, Queen Mary University of London, Mile End Road, London, E1 4NS, UK*

(Dated: February 11, 2026)

We introduce a novel observable associated to Abelian monopole currents defined in the Maximal Abelian Projection of SU(3) Yang-Mills theory that captures the topology of the current loop. This observable, referred to as the *simplicity*, is defined as the ratio of the zeroth over the first Betti number of the current graph for a given field configuration. A numerical study of the expectation value of the simplicity performed in the framework of Lattice Gauge Theories enables us to determine the deconfinement temperature to a higher degree of accuracy than that reached by conventional methods at a comparable computational effort. Our results suggest that Abelian current loops are strongly correlated with the degrees of freedoms of the theory that determine confinement. Our investigation opens new perspectives for the definition of an order parameter for deconfinement in Quantum Chromodynamics able to expose the potentially rich phase structure of the theory.

Introduction — The problem of colour confinement in the strong interactions, i.e., the absence of fractionally charged particles in asymptotic states, is broadly acknowledged as one of the most urgent gaps to fill in order to gain a full understanding of Quantum Chromodynamics (QCD) and, more in general, of the dynamics of non-Abelian gauge theories. It is known that at high temperature confinement is lost. The widely accepted scenario (for a recent review, see, e.g., Ref. [1]) is that above a critical temperature the system behaves as a plasma of its elementary constituents, quarks and gluons. This picture has recently been challenged, and the suggestion that an intermediate regime separates the confinement regime from the deconfined quark-gluon-plasma one (see, e.g., Refs. [2–7]) is gaining increasing consensus. In the light of this development, a full characterisation of confinement appears to be even more crucial. To study QCD, a first-principles approach that has been used, often in conjunction with analytic guidance, is Lattice Gauge Theory, of which the demonstration of confinement through the area law of Wilson loops has been the very first application [8].

It is an old idea that confinement can be understood in terms of the dynamics of topological excitations carrying a non-trivial magnetic charge [9, 10]. This has led to the proposal of defining Abelian magnetic monopoles through a partial gauge fixing procedure known as *Abelian projection* [11]. A number of studies were performed which explored these ideas from various angles [12–14], from dominance of degrees of freedom that are Abelian in certain projections [15] to the construction of disorder parameters [16–18]¹ and effec-

tive monopole potentials [21]. Studies of the gauge-independence of monopole condensation [22] and investigations of thermal monopole properties [23, 24] provided important insights into the connection between monopole dynamics and the confinement/deconfinement transition, with an approach based on an effective model for the condensation of monopoles at the critical temperature [25] enabling the computation of the latter in SU(2) Yang-Mills [26]. More recent investigations [27, 28] reaffirmed the centrality of monopoles in colour confinement.

Despite this noticeable progress, we still lack a robust (dis)order parameter for confinement in Yang-Mills theory based on features of these topological excitations that is free from lattice artefacts, enables determining with sufficient accuracy quantities that characterise the dynamics of the transition, and can be readily adopted in the presence of dynamical fermions. A key difficulty is the topological nature of monopole excitations, which is harder to expose in the lattice discretisation. Recently, Topological Data Analysis (TDA) has emerged in computational topology as a robust methodology to characterise topological properties of discrete sets of points. For this reason, applications of TDA to field theory and statistical mechanics are raising at a fast pace (see, e.g., [29–38]). Building on the intuition developed from previous studies and borrowing rigorous tools of TDA along the path laid in Refs. [39, 40], in this letter we are going to propose and test in SU(3) Yang-Mills an observable derived from magnetic monopole currents that quantitatively characterises the deconfinement phase transition. We will demonstrate numerically that this observable, whose definition in the presence of fermions remains identical, enables us to accurately determine the critical value of the coupling and the order of the phase transition in the pure gauge system, henceforth providing evidence of the relevance of Abelian monopoles for deconfinement in Yang-Mills.

¹ Pathologies identified in the original disorder parameter construction [19] led to the improved proposal [20].

SU(3) Yang-Mills on the Lattice — We consider the SU(3) lattice gauge theory described by the Wilson action,

$$S = \beta \sum_i \sum_{\mu < \nu} \left[1 - \frac{1}{3} \Re \text{Tr} U_{\mu\nu}(i) \right], \quad (1)$$

with $\beta \equiv 6/g^2$ and g the coupling of the theory. This action becomes the Yang-Mills action in the continuum limit. The quantity

$$U_{\mu\nu}(i) \equiv U_\mu(i) U_\nu(i + \hat{\mu}) U_\mu^\dagger(i + \hat{\nu}) U_\nu^\dagger(i) \quad (2)$$

is the plaquette variable, with $U_\mu(i) \in \text{SU}(3)$ the link variable, defined on the link $(i; \hat{\mu})$ stemming from the point i and ending at the point $i + \hat{\mu}$ (with $\hat{\mu}$ the unit vector in the positive direction μ) of a four-dimensional Euclidean lattice of dimension $N_t \times N_s^3$. Periodic boundary conditions are imposed in all directions. The temperature T of the system is given by

$$T = \frac{1}{a(\beta) N_t}, \quad (3)$$

with $a(\beta)$ the lattice spacing, which is a monotonically decreasing function of β . The path integral is given by

$$Z = \int \left(\prod_{i,\mu} dU_\mu(i) \right) \exp\{-S\}, \quad (4)$$

with $dU_\mu(i)$ representing the Haar measure.

At thermal equilibrium, the expectation value of a given observable O is computed using

$$\langle O \rangle = \frac{1}{Z} \int \left(\prod_{i,\mu} dU_\mu(i) \right) O \exp\{-S\}. \quad (5)$$

By fixing N_t and taking the infinite volume limit $N_s \rightarrow \infty$, we can study the system's behaviour in the thermodynamic limit. The thermodynamic observables thus extracted can then be extrapolated to the continuum limit by taking progressively finer discretisations in N_t .

Magnetic monopoles in the Maximal Abelian Gauge —

The identification of Abelian magnetic monopole currents in $\text{SU}(N)$ gauge theories is performed following a gauge-fixing procedure known as an *Abelian projection*. To define an Abelian projection, an operator F transforming in the adjoint representation is chosen, and a partial gauge fixing is performed. The latter consists in diagonalising F at each point and ordering its eigenvalues $\lambda_1, \dots, \lambda_N$ in non-decreasing order. This partial gauge fixing leaves a residual $\text{U}(1)^{N-1}$ symmetry. The process exposes $N-1$ species of magnetic monopoles, each corresponding to one of the $\text{U}(1)$ residual gauge factors. Magnetic monopoles of the type j occur where $\lambda_j = \lambda_{j+1}$. In $\text{SU}(3)$ Yang-Mills, we then have two types of monopoles.

While the gauge-dependence of the identification of monopole currents might obscure the gauge-invariant picture, physical properties of magnetic monopoles in some gauge can be a useful starting point to better understand properties of more complex underlying topological structures that the gauge-dependent objects exemplify. In this respect, a particularly useful gauge is the Maximal Abelian Gauge (*MAG*), since gauge-independent excitations maximally overlap with Abelian monopoles defined in this gauge [41]. Following the prescription of Ref. [42], for the $\text{SU}(3)$ lattice Yang-Mills theory, we define the adjoint operator $\tilde{X}(i)$ as

$$\tilde{X}(i) = \sum_\mu \left[U_\mu(i) \tilde{\lambda} U_\mu^\dagger(i) + U_\mu^\dagger(i - \hat{\mu}) \tilde{\lambda} U_\mu(i - \hat{\mu}) \right], \quad \tilde{\lambda} = \text{diag}(1, 0, -1). \quad (6)$$

The MAG is defined as the gauge in which $\tilde{X}(i)$ is diagonal. This gauge choice is equivalent to requiring that the operator

$$\tilde{F}_{\text{MAG}}(U, g) = \sum_{\mu, i} \text{tr} \left(g(i) U_\mu(i) g^\dagger(i + \hat{\mu}) \tilde{\lambda} g(i + \hat{\mu}) U_\mu^\dagger(i) g^\dagger(i) \tilde{\lambda} \right) \quad (7)$$

is maximised over g , i.e., the gauge fixing transformation $\{g\}$ can be derived from the condition

$$\{\tilde{g}\} = \underset{\{g\}}{\text{argmax}} \tilde{F}_{\text{MAG}}(U, g). \quad (8)$$

In the MAG, the diagonal elements of the link matrices

\tilde{U}_{ii} read

$$\tilde{U}_{ii} = r_i e^{i\varphi_i}, \quad \sum_i \varphi_i = 2\pi n + \delta\varphi. \quad (9)$$

In general, $\delta\varphi \neq 0$, as a consequence of the fact that even after gauge fixing the links are not fully diagonal. Angle variables ϕ_i are then defined through the redistribution

of the excess phase as

$$\phi_i = \varphi_i - \delta\varphi \frac{\left| \tilde{U}_{ii} \right|^{-1}}{\sum_j \left| \tilde{U}_{jj} \right|^{-1}}. \quad (10)$$

The two lattice Abelian fields in the residual gauge are $\theta_1 = \phi_1$ and $\theta_2 = -\phi_3$. The corresponding species of monopoles are defined following the prescription of Ref. [43]. The truncation of the theory to the degrees of freedom represented by these two angles provides a definition of *Abelian projection* using the MAG.

Topological simplicity — To investigate the topology of monopole currents, it is convenient to define the dual lattice Λ^* , obtained by shifting each point by half a lattice spacing in all positive directions. Each geometric element of the original lattice Λ of dimension d is pierced at its centre by an element of Λ^* of dimension $4 - d$. These two elements are dual to each other. Being defined on cubes of Λ , on Λ^* magnetic charges are link variables and are more appropriately referred to as currents. For each lattice configuration, each dual link $(j; \hat{\mu})$ carries a current $m_\mu(j) = 0, \pm 1, \pm 2$. A non-trivial current m on the dual link $(j; \hat{\mu})$ can be seen as a charge m moving from site j to site $j + \hat{\mu}$. Akin to Kirchoff's law, the total charge entering a dual site j is equal to the total charge exiting from that site. For the same reason, currents cannot end at sites but must form closed loops. The set of links $G \equiv \{(j; \hat{\mu}), m_\mu(j) \neq 0\}$ is the current graph associated to the configuration on which the $m_\mu(j)$ have been computed. This object is interpreted as a graph, with vertices coinciding with the end points of links in G and edges coinciding with the links in G . The number of connected components of G defines the Betti number b_0 , while the total number of loops defines the Betti number b_1 . In [40], we have shown that both quantities

$$\rho_0 = \frac{\langle b_0 \rangle}{N_s^3} \quad \text{and} \quad \rho_1 = \frac{\langle b_1 \rangle}{N_s^3} \quad (11)$$

are sensitive to the phase transition, by providing numerical evidence that their susceptibilities, χ_0 and χ_1 , display a peak at a value $\beta_c(N_s, N_t)$ of β that for fixed N_t scales as

$$\beta_c(N_s, N_t) = \beta_c(N_t) + a/N_s^3, \quad (12)$$

where $\beta_c(N_t)$ is the critical value of β at fixed N_t . While these results show a remarkable connection between topological properties of current graphs and the deconfinement phase transition, suggesting that expectation values of the Betti numbers b_0 and b_1 are key to understanding confinement, they fail short of providing an order parameter for the deconfinement phase transition.

In this work, we use the information above and expectations developed from previous calculations to define a

N_t	N_s	β_{\min}	β_{\max}	N_β	N_{meas}
4	16, 20, 24, 28, 32	5.6600	5.7200	15	600
6	24, 30, 36, 42, 48	5.8100	5.9300	12	600
8	32, 40, 48, 56, 64	6.0350	6.0800	12	400

TABLE I. This table specifies the various lattice sizes, N_t and N_s , that we use in this study. For $N_t = 4$, we draw a sample of $N = 600$ configurations, for a range of 15 β values. For $N_t = 6$, we draw a sample of $N = 600$ configurations, for a range of 12 β values. For $N_t = 8$, we draw a sample of $N = 400$ configurations, for a range of 12 β values.

quantity that behaves as an order parameter. This observable is the *topological simplicity*, or just *simplicity*, which is defined as

$$\lambda = \left\langle \frac{b_0}{b_1} \right\rangle. \quad (13)$$

The ratio that defines this observable, $\frac{b_0}{b_1}$, is the reciprocal of the number of loops per connected component, which is sometimes called the *complexity* and is at least 1. While the simplicity and complexity are undefined for an empty network, a typical configuration at non-infinite β will have a non-empty monopole network. In the confined phase at low temperature (corresponding at fixed N_t to low β), one typically sees a percolating current network with one component and many loops, and so the simplicity approaches 0. In the deconfined phase at high temperature (corresponding at fixed N_t to high β), large fluctuations are suppressed by the Boltzmann weight and dominant configurations have current networks consisting of a sparse gas of loops, so the simplicity is approximately 1. In the critical region, due to the breaking of the percolating loop, the simplicity raises from 0 to 1.

However, this qualitative behaviour is not sufficient to evidence the coupling of λ with the degrees of freedom that are relevant for the phase transition. In order to test whether λ is an observable that is sensitive to the deconfinement phase transition, we study the behaviour of its susceptibility

$$\chi_\lambda = V \left(\left\langle \left(\frac{b_0}{b_1} \right)^2 \right\rangle - \left\langle \frac{b_0}{b_1} \right\rangle^2 \right) \quad (14)$$

in a range of β values in the critical region, for a range of spatial extensions N_s and temporal extensions $N_t = 4, 6, 8$, as specified in Tab. I. Larger values of N_t correspond to finer discretisations of the direction associated with the temperature (see Eq. (3)). Varying N_s will instead enable us to prove sensitivity to the expected first-order deconfinement phase transition, which will be shown by the detection of the scaling behaviour in Eq. (12).

We report in Fig. 1 the behaviour of λ and of χ_λ together with a determination for β_c for $N_t = 8$ with

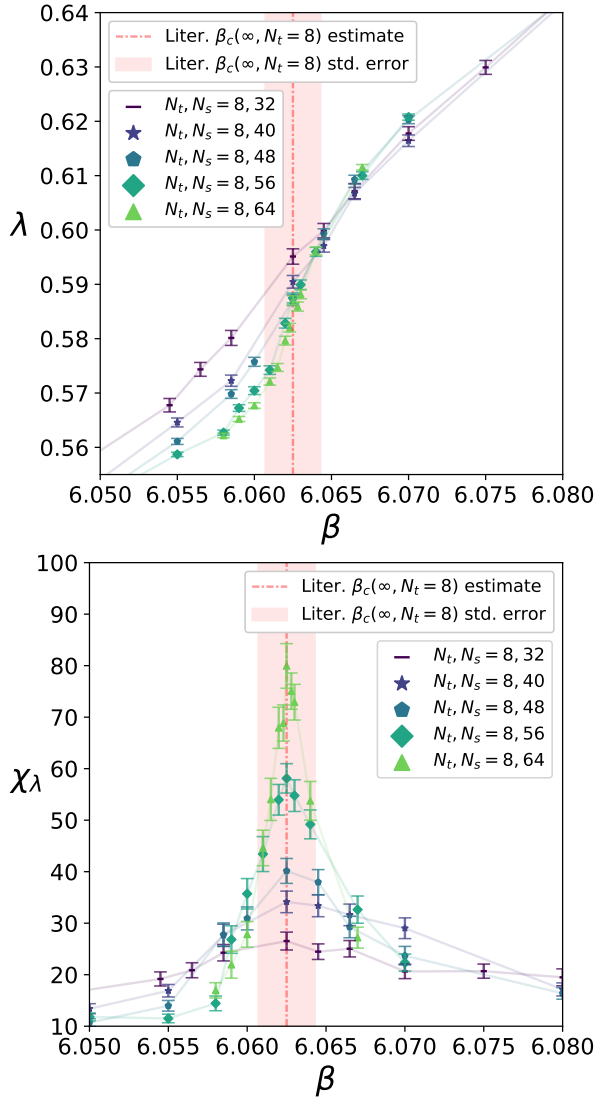


FIG. 1. For $N_t = 8$, λ and χ_λ as functions of β zoomed into the critical region with translucent lines to guide the eye. The vertical line and band show respectively the central value and the statistical error for the extrapolated β_c determined in Ref. [44].

conventional methods taken from Ref. [44]. λ shows a monotonically increasing behaviour, with slope that gets steeper near β_c and becomes more pronounced as the volume increases. As a consequence, the susceptibility χ_λ has a peak in the critical region with height growing with the volume. Figs. 2, 3 and 4 show the scaling of the position of the peak of χ_λ with the spatial volume, respectively at $N_t = 4, 6, 8$. The data have been fitted with Eq. (12) and with a higher-order correction in $1/N_s^3$ for various fitting ranges, and the results have been combined with the Akaike information principle in the implementation of Ref. [45] to determine a weighted extrapolation and the corresponding errors (both also reported in the figures).

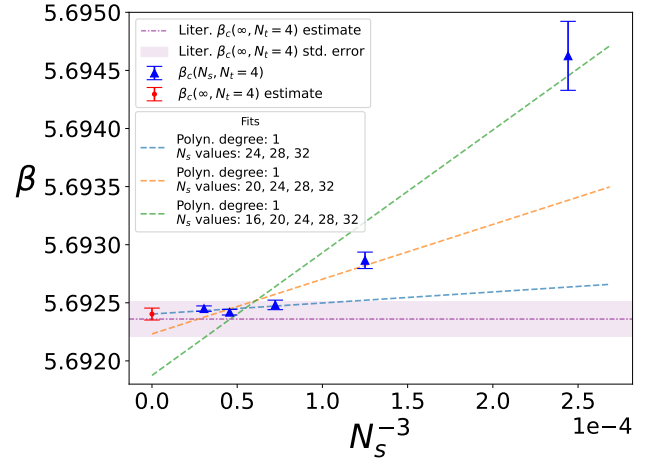


FIG. 2. Position of the peak of χ_λ for lattices with $N_t = 4$ and $N_s = 16, 20, 24, 28, 32$ (blue triangles). Dashed lines represent the polynomial regression fits used for the infinite volume extrapolation of these peak values, and the red circle is the resulting estimate of β_c in the thermodynamic limit (see the supplemental material for additional details). The horizontal line and band show respectively the central value and the statistical error for the extrapolated β_c determined in Ref. [44].

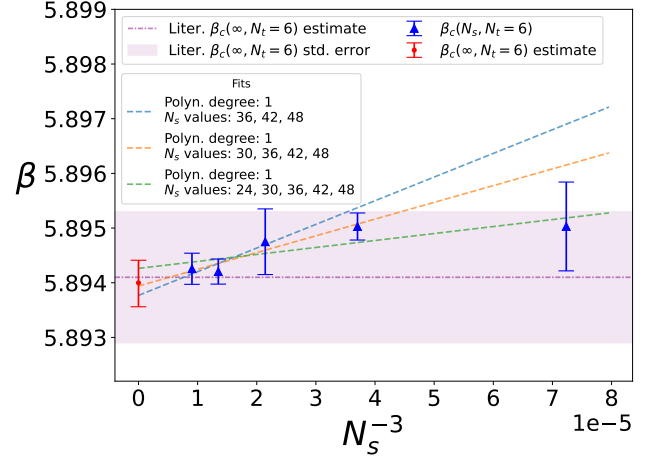


FIG. 3. Position of the peak of χ_λ for lattices with $N_t = 6$ and $N_s = 24, 30, 36, 42, 48$ (blue triangles). Dashed lines represent the polynomial regression fits used for the infinite volume extrapolation of these peak values, and the red circle is the resulting estimate of β_c in the thermodynamic limit (see the supplemental material for additional details). The horizontal line and band show respectively the central value and the statistical error for the extrapolated β_c determined in Ref. [44].

Discussion and outlook — The smaller error bar of the extrapolated value with respect to the reference value, which has been obtained by averaging over around an order of magnitude more configurations, provides evidence of the relevance of the topological properties captured by the simplicity for the dynamics of colour confinement.

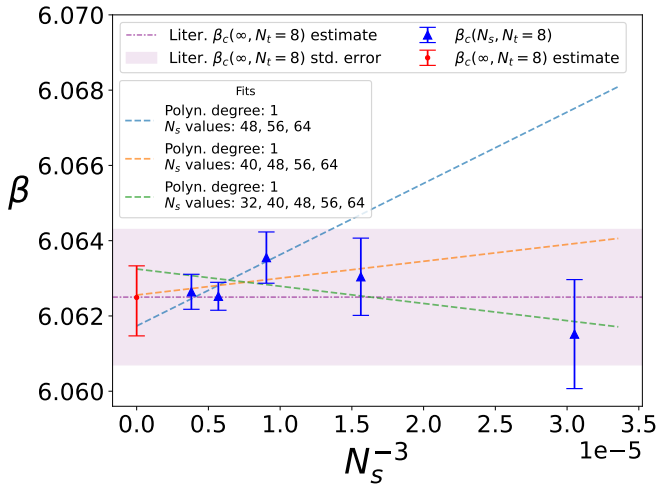


FIG. 4. Position of the peak of χ_λ for lattices with $N_t = 8$ and $N_s = 32, 40, 48, 56, 64$ (blue triangles). Dashed lines represent the polynomial regression fits used for the infinite volume extrapolation of these peak values, and the red circle is the resulting estimate of β_c in the thermodynamic limit (see the supplemental material for additional details). The horizontal line and band show respectively the central value and the statistical error for the extrapolated β_c determined in Ref. [44].

We remark that the simplicity can be adopted also in the presence of dynamical fermions. If a novel intermediate-temperature behaviour exists in QCD, based on our studies of spin systems, where observables constructed with similar methodology as the simplicity have proved to be sensitive to the order-disorder phase transition, we expect the susceptibility of the simplicity to show a non-monotonic structure at the higher-temperature change of regime.

Acknowledgements — We thank M. D’Elia, A. Gonzalez-Arroyo and T. Sulejmanpasic for discussions. XC was supported by the Additional Funding Programme for Mathematical Sciences, delivered by EPSRC (EP/V521917/1) and the Heilbronn Institute for Mathematical Research. JG was supported by EPSRC grant EP/R018472/1 through the Centre for TDA and the Erlangen Hub for AI through EPSRC grant EP/Y028872/1. The work of BL was partly supported by the EPSRC ExCALIBUR ExaTEPP project EP/X017168/1 and by the STFC Consolidated Grants No. ST/T000813/1 and ST/X000648/1.

Numerical simulations have been performed on the Swansea SUNBIRD cluster (part of the Supercomputing Wales project) and AccelerateAI A100 GPU system. The Swansea SUNBIRD system and AccelerateAI are part funded by the European Regional Development Fund (ERDF) via Welsh Government.

This work used the DiRAC Data Intensive service (CSD3) at the University of Cambridge, managed by the University of Cambridge University Information Ser-

vices on behalf of the STFC DiRAC HPC Facility (www.dirac.ac.uk). The DiRAC component of CSD3 at Cambridge was funded by BEIS, UKRI and STFC capital funding and STFC operations grants. DiRAC is part of the UKRI Digital Research Infrastructure.

Open Access Statement — For the purpose of open access, the authors have applied a Creative Commons Attribution (CC BY) licence to any Author Accepted Manuscript version arising.

Research Data Access Statement — The data and analysis code for this manuscript can be downloaded from Ref. [46]. The Monte Carlo code can be found from Ref. [47].

* 2237451@swansea.ac.uk

† jeffrey.giansiracusa@durham.ac.uk

‡ b.lucini@qmul.ac.uk

- [1] G. Aarts *et al.*, *Prog. Part. Nucl. Phys.* **133**, 104070 (2023), arXiv:2301.04382 [hep-lat].
- [2] L. Y. Glozman, *Acta Phys. Polon. Supp.* **10**, 583 (2017), arXiv:1610.00275 [hep-lat].
- [3] A. Alexandru and I. Horváth, *Phys. Rev. D* **100**, 094507 (2019), arXiv:1906.08047 [hep-lat].
- [4] M. Cardinali, M. D’Elia, and A. Pasqui, arXiv:2107.02745 [hep-lat] (2021), arXiv:2107.02745.
- [5] M. Hanada, H. Ohata, H. Shimada, and H. Watanabe, *PTEP* **2024**, 041B02 (2024), arXiv:2310.01940 [hep-th].
- [6] Y. Fujimoto, K. Fukushima, Y. Hidaka, and L. McLerran, *Phys. Rev. D* **112**, 074006 (2025), arXiv:2506.00237 [hep-ph].
- [7] J. A. Mickley, C. Allton, R. Bignell, and D. B. Leinweber, *Phys. Rev. D* **112**, 054505 (2025), arXiv:2507.17200 [hep-lat].
- [8] K. G. Wilson, *Phys. Rev. D* **10**, 2445 (1974).
- [9] S. Mandelstam, *Phys. Rept.* **23**, 245 (1976).
- [10] G. ’t Hooft, in *New Phenomena in Subnuclear Physics*, edited by A. Zichichi (Editrice Compositori, Bologna, 1976) pp. 1225–1249, proceedings of the talk given at the 13th International School of Subnuclear Physics: New Phenomena in Subnuclear Physics, 11 July–1 August 1975. Erice, Italy.
- [11] G. ’t Hooft, *Nucl. Phys. B* **190**, 455 (1981).
- [12] A. S. Kronfeld, G. Schierholz, and U. J. Wiese, *Nucl. Phys. B* **293**, 461 (1987).
- [13] A. S. Kronfeld, M. L. Laursen, G. Schierholz, and U. J. Wiese, *Phys. Lett. B* **198**, 516 (1987).
- [14] T. L. Ivanenko, A. V. Pochinsky, and M. I. Polikarpov, *Phys. Lett. B* **302**, 458 (1993).
- [15] Z. F. Ezawa and A. Iwazaki, *Phys. Rev. D* **25**, 2681 (1982).
- [16] L. Del Debbio, A. Di Giacomo, G. Paffuti, and P. Pieri, *Phys. Lett. B* **355**, 255 (1995), arXiv:hep-lat/9505014.
- [17] A. Di Giacomo, B. Lucini, L. Montesi, and G. Paffuti, *Phys. Rev. D* **61**, 034503 (2000), arXiv:hep-lat/9906024.
- [18] A. Di Giacomo, B. Lucini, L. Montesi, and G. Paffuti, *Phys. Rev. D* **61**, 034504 (2000), arXiv:hep-lat/9906025.
- [19] J. Greensite and B. Lucini, *Phys. Rev. D* **78**, 085004 (2008), arXiv:0806.2117 [hep-lat].
- [20] C. Bonati, G. Cossu, M. D’Elia, and A. Di Giacomo,

Phys. Rev. D **85**, 065001 (2012), arXiv:1111.1541 [hep-lat].

[21] M. N. Chernodub, M. I. Polikarpov, and A. I. Veselov, Phys. Lett. B **399**, 267 (1997), arXiv:hep-lat/9610007.

[22] J. M. Carmona, M. D’Elia, A. Di Giacomo, B. Lucini, and G. Paffuti, Phys. Rev. D **64**, 114507 (2001), arXiv:hep-lat/0103005.

[23] M. N. Chernodub and V. I. Zakharov, Phys. Rev. Lett. **98**, 082002 (2007), arXiv:hep-ph/0611228.

[24] A. D’Alessandro and M. D’Elia, Nucl. Phys. B **799**, 241 (2008), arXiv:0711.1266 [hep-lat].

[25] M. Cristoforetti and E. Shuryak, Phys. Rev. D **80**, 054013 (2009), arXiv:0906.2019 [hep-ph].

[26] A. D’Alessandro, M. D’Elia, and E. V. Shuryak, Phys. Rev. D **81**, 094501 (2010), arXiv:1002.4161 [hep-lat].

[27] M. Nguyen, T. Sulejmanpasic, and M. Ünsal, Phys. Rev. Lett. **134**, 141902 (2025), arXiv:2401.04800 [hep-th].

[28] J. Giansiracusa, D. Lanners, and T. Sulejmanpasic, Phys. Rev. Lett. **135**, 221901 (2025).

[29] I. Donato, M. Gori, M. Pettini, G. Petri, S. De Nigris, R. Franzosi, and F. Vaccarino, Phys. Rev. E **93**, 052138 (2016), arXiv:1601.03641.

[30] Q. H. Tran, M. Chen, and Y. Hasegawa, Phys. Rev. E **103**, 052127 (2021), arXiv:2004.03169 [cond-mat.stat-mech].

[31] K. Kashiwa, T. Hirakida, and H. Kouno, Symmetry **14**, 1783 (2022), arXiv:2103.12554 [hep-lat].

[32] B. Olsthoorn, J. Hellsvik, and A. V. Balatsky, Phys. Rev. Res. **2**, 043308 (2020), arXiv:2009.05141 [cond-mat.stat-mech].

[33] A. Cole, G. J. Loges, and G. Shiu, Phys. Rev. B **104**, 104426 (2021), arXiv:2009.14231 [cond-mat.stat-mech].

[34] N. Sale, J. Giansiracusa, and B. Lucini, Phys. Rev. E **105**, 024121 (2022), arXiv:2109.10960 [cond-mat.stat-mech].

[35] D. Sehayek and R. G. Melko, Phys. Rev. B **106**, 085111 (2022), arXiv:2201.09856 [cond-mat.stat-mech].

[36] N. Sale, B. Lucini, and J. Giansiracusa, Phys. Rev. D **107**, 034501 (2023), arXiv:2207.13392 [hep-lat].

[37] D. Spitz, J. M. Urban, and J. M. Pawłowski, Phys. Rev. D **107**, 034506 (2023), arXiv:2208.03955 [hep-lat].

[38] D. Spitz, J. M. Urban, and J. M. Pawłowski, Phys. Rev. D **111**, 114519 (2025), arXiv:2412.09112 [hep-lat].

[39] X. Crean, J. Giansiracusa, and B. Lucini, SciPost Phys. **17**, 100 (2024), arXiv:2403.07739 [hep-lat].

[40] X. Crean, J. Giansiracusa, and B. Lucini, PoS **LAT-TICE2024**, 395 (2025), arXiv:2501.19320 [hep-lat].

[41] C. Bonati, A. Di Giacomo, L. Lepori, and F. Pucci, Phys. Rev. D **81**, 085022 (2010), arXiv:1002.3874 [hep-lat].

[42] C. Bonati and M. D’Elia, Nucl. Phys. B **877**, 233 (2013), arXiv:1308.0302 [hep-lat].

[43] T. A. DeGrand and D. Toussaint, Phys. Rev. D **22**, 2478 (1980).

[44] B. Lucini, M. Teper, and U. Wenger, JHEP **2004** (01), 061, arXiv:hep-lat/0307017.

[45] W. I. Jay and E. T. Neil, Phys. Rev. D **103**, 114502 (2021), arXiv:2008.01069 [stat.ME].

[46] X. Crean, J. Giansiracusa, and B. Lucini, Simplicity of confinement in $SU(3)$ Yang-Mills theory — Data and Analysis Code Release (2026).

[47] X. Crean, J. Giansiracusa, and B. Lucini, Simplicity of confinement in $SU(3)$ Yang-Mills theory — Monte Carlo Code Release (2026).

[48] N. Cabibbo and E. Marinari, Phys. Lett. B **119**, 387 (1982).

[49] P. Dlotko, in *GUDHI User and Reference Manual* (GUDHI Editorial Board, 2015).

[50] A. M. Ferrenberg and R. H. Swendsen, Phys. Rev. Lett. **63**, 1195 (1989).

[51] M. Luscher, Comput. Phys. Commun. **79**, 100 (1994), arXiv:hep-lat/9309020.

Supplemental Material: Simplicity of confinement in SU(3) Yang-Mills theory

Xavier Crean,¹ Jeffrey Giansiracusa,² and Biagio Lucini³

¹*Department of Mathematics, Faculty of Science and Engineering,
Swansea University, Fabian Way, Swansea, SA1 8EN, UK*

²*Department of Mathematical Sciences, Durham University,
Upper Mountjoy Campus, Durham, DH1 3LE, UK*

³*School of Mathematical Sciences, Queen Mary University of London,
Mile End Road, London, E1 4NS, UK*

Topological Data Analysis for Lattice Gauge Theories

Topology is about quantifying the aspects of shapes that are invariant under stretching and deforming. Topological data analysis (TDA) emerged from this domain as a set of computational tools that produce numerical invariants of the shape of objects arising from data. These numerical invariants can provide insight into the shape of the distribution underlying a set of samples. We take a different approach here, using TDA tools to produce non-local observables for lattice gauge theories that are sensitive to large scale structures appearing in configurations.

In algebraic topology, one frequently represents geometric objects with simplicial complexes. However, since we are working with lattice gauge theory on cubical lattices, it is more convenient to represent geometric objects as cubical complexes, which are simply objects built by gluing cubes together along their boundaries.

One of the fundamental algebraic invariants of topology is *homology*, which is about quantifying the holes and voids of a shape. Holes come in different types. A point missing from the plane is a 1-dimensional hole in the sense that it can be captured by a circle, which is a 1-dimensional manifold. However, a circle cannot capture a point missing from 3-space because it could always slip off over the top or bottom; this hole must be wrapped by a sphere, which is a 2-dimensional manifold, so this is a 2-dimensional hole. Homology formalises this idea. The input is a simplicial or cubical complex X . The output is a vector space $H_n(X)$ for each natural number n . The dimension of $H_n(X)$ represents the count of n -dimensional holes. Here are some useful properties of homology.

1. If X is a point (or contractible), then $H_0(X)$ is 1-dimensional, and $H_n(X) = 0$ (the trivial vector space) for all $n > 0$.
2. In general, $H_0(X)$ has dimension equal to the number of connected components of X .
3. Disjoint union $X \cup Y$ corresponds to direct sum: $H_n(X \cup Y) \cong H_n(X) \oplus H_n(Y)$.
4. $H_n(X) = 0$ for all n larger than the dimension of X .
5. If X is a d -dimensional closed and orientable manifold, then $H_d(X)$ is 1-dimensional.
6. If X and Y are homotopy equivalent, then $H_i(X) \cong H_i(Y)$ for all i .

In some situations, having a vector space is more information than just having its dimension. However, in this paper we will only make use of the dimensions. The dimension of $H_i(X)$ is known as the i th Betti number of X , and it is denoted b_i .

Cubical complexes

An n -dimensional cube is simply a Cartesian product of n copies of the unit interval $[0, 1]$. More systematically, given a finite set A , the associated cube $C(A)$ is $[0, 1]^A$. Let $(x_a)_{a \in A}$ be coordinates on the cube. A *face* of this cube is a subspace where some collection of coordinates x_a are either 0 or 1. Each face is canonically linearly homeomorphic to a cube of lower dimension.

An orientation of a cube $C(A)$ corresponds to a choice of ordering of the set A up to even permutations. Since a cube is a manifold with boundary and corners, an orientation of $C(A)$ induces an orientation of each codimension 1 face. In terms of orderings, the induced orientation of the face at $x_a = 0$ is given by representing the orientation as

an ordering of A with a last and then restricting this to an ordering of $A \setminus \{a\}$, and the induced orientation of the opposite face at $x_a = 1$ is given by the opposite of this.

A *cubical complex* is a topological space X together with a collection of maps $\{f_i : C_i \rightarrow X\}$ of cubes C_i into X , satisfying the following conditions:

1. Each f_i is a homeomorphism onto its image.
2. The union of the images is all of X .
3. If the images of f_i and f_j have non-empty intersection K , then the composition of f_i (restricted to the preimage of K) followed by f_j^{-1} is a linear homeomorphism of a face of C_i onto a face of C_j .

A *subcomplex* is a subspace of X that is the union of the images of a subset of the cubes.

The example we are concerned with here is the cubical complex corresponding to a dual lattice Λ^* for a lattice discretisation of spacetime Λ and subcomplexes corresponding to a collection of links.

Chain complexes and their homology

A *chain complex* is a sequence of vector spaces and linear maps

$$\dots \xrightarrow{\partial_{d+1}} V_d \xrightarrow{\partial_d} V_{d-1} \xrightarrow{\partial_{d-1}} V_{d-2} \longrightarrow \dots$$

such that the compositions $\partial_d \circ \partial_{d+1}$ are all equal to 0.

Given a cubical complex $(X, \{f_i : C_i \rightarrow X\})$, which we abbreviate simply as X , one obtains a chain complex as follows. The degree d space V_d is spanned by the pairs

$$(C_i \text{ an } d\text{-cube of } X, o \text{ an orientation on } C_d)$$

modulo the relation that $-(C, o) = (C, -o)$. The boundary map ∂_d sends (C, o) to the sum of the codimension 1 faces of C with their induced orientations.

Note that if all vector spaces are defined over the field $\mathbb{Z}/2$, then one doesn't need to keep track of orientations and signs, as $(C, o) = (C, -o)$.

Homology

Elements in the kernel of ∂_d are called *cycles* in degree d , and the subspace of cycles is written Z_d . Elements in the image of ∂_{d+1} are called *boundaries* of degree d , and the space of boundaries is B_d . Every boundary is a cycle, so $B_d \subset Z_d$, but the converse is not necessarily true. The homology H_d is defined to be the quotient vector space Z_d/B_d . It measures the extent to which there are cycles that are not boundaries.

The above algebraic definition may not appear all that intuitive, but it has the advantage that it can easily be turned into an algorithm to produce a basis for the homology in any given degree and hence determine the Betti numbers.

Graphs

A graph (without edges that start and end at the same vertex) is an example of a cubical complex. In fact, these are the only kind of cubical complexes that we need to consider in this paper.

If X is a graph, then the homology is nontrivial only in degrees 0 and 1. The degree 0 part tells us the number of connected components, which is the *zeroth Betti number*, b_0 . If G is a connected graph and $T \subset G$ is a spanning tree (a subgraph that is a tree with the property that adding any additional edge of G to T results in it no longer being a tree), then contracting all the edges of T results in a single vertex v and a collection of loop edges that start and end at v , one for each edge in the complement of T . See Fig. S1. Since the spanning tree T is a tree, and hence contractible, the original graph G is homotopy equivalent to the result of contracting T .

One can show that the *first Betti number*, b_1 , (the dimension of $H_1(G)$) is equal to the number of edges in the complement of a spanning tree, which is the number of loops in G/T .

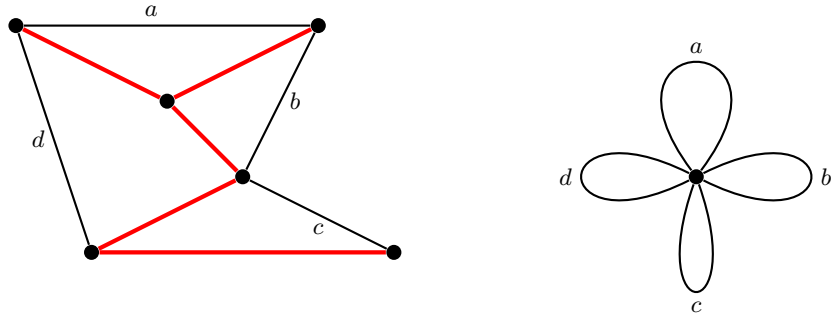


FIG. S1. Left: A graph G and a spanning tree T shown in red. Right: the graph G/T resulting from contracting T to a single vertex.

Monte Carlo simulations

In this study, we draw a sample of $SU(3)$ lattice gauge field configurations using MCMC importance sampling methods, namely the heat-bath and overrelax algorithms [48]. We define one composite update as 1 heat-bath update followed by 4 overrelax updates. Note that importance sampling reliably approximates the system's Boltzmann distribution once the Markov chain has been successfully equilibrated; thus, for every simulation, we discard the first 10,000 composite updates. Further, in order to minimise the autocorrelation between successive recorded configurations, we separate each recording by 2,000 composite updates. For each respective lattice size, we select an appropriate range of β values to study that are strategically located to cover the critical region of the deconfinement transition; this has been previously specified in the literature, e.g., in Ref. [44]. For each β value in our selected range, we record a sample of N_{meas} configurations. Using our given computational allocation, we have been able to record $N_{\text{meas}} = 600$ configurations for lattices with $N_t = 4, 6$ and $N_{\text{meas}} = 400$ configurations for lattices with $N_t = 8$. Thermal expectation values of observables, as per Eq. (5), are then estimated as the sample mean as a function of β . We estimate the standard error in the sample mean by using the bootstrap method with $N_{\text{bs}} = 2,000$. Further details on our computational pipeline can be seen in this publication's accompanying code release in Ref. [46].

Data analysis

In this work, we analyse the union of the Abelian magnetic monopole currents – treating both species on an equal footing. We have verified that considering each individual species produces compatible results to the analysis of the union of species. Further, we observe no statistically significant difference between the two species – this is consistent with the picture seen in the literature, e.g., Refs. [4, 40, 42].

Our aim is to analyse readily computable topological invariants of the monopole current networks called Betti numbers. By fixing an arbitrary orientation (the results are independent of this choice), we map the network of monopole currents to a directed graph G . We then compute $b_0(G) \equiv \dim H_0(G)$ representing the components of the graph and $b_1(G) \equiv \dim H_1(G)$ representing the number of loops in the graph. In our computation of $b_k(G)$, we leverage a highly optimised implementation of a homology computing algorithm, namely Ref. [49], designed to deal with a cubical complex. This is possible since a directed graph is a 1-dimensional cubical complex; therefore, a cubical complex is a convenient data structure for representing graphs. See Ref. [39], for further details.

Our results for $\rho_i(\beta)$ and $\chi_i(\beta)$ (as defined in the main body) at $N_t = 4, 6, 8$ are plotted in Figs. S2, S3, S4, S5, S6 and S7 respectively. A suitable range of β -values covering the critical region have been chosen with error bars computed using the bootstrap method with $N_{\text{bs}} = 2,000$. One can see that the susceptibilities χ_i peak at the critical value with peaks becoming larger and more concentrated as the spatial volume increases as expected for an extensive observable at the critical value of a first order phase transition.

Similarly, our results for the simplicity $\lambda(\beta)$ and $\chi_\lambda(\beta)$ for $N_t = 4, 6, 8$ are plotted in Figs. S8, S9 and 1 respectively. One can see that the susceptibility χ_λ peaks at the critical value with peaks becoming larger and more concentrated as the spatial volume increases. In Fig. S10, we plot a wider range of β -values for $N_t, N_s = 8, 32$ so that the global trend is made clear for finite N_s size.

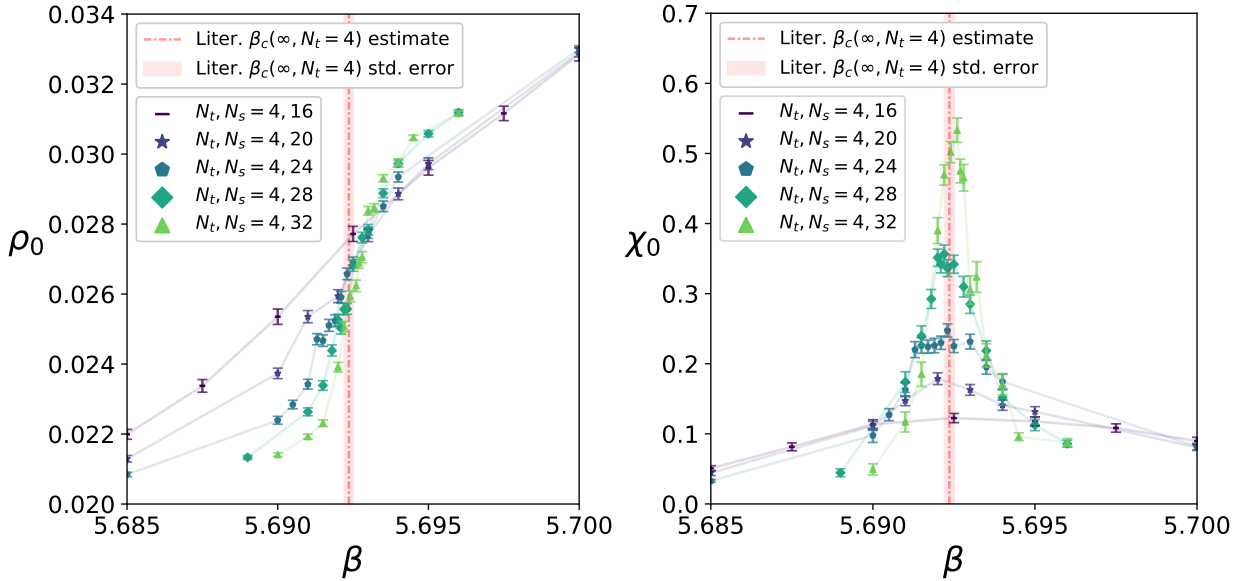


FIG. S2. For $N_t = 4$, a scatter plot of ρ_0 and χ_0 as functions of β with translucent lines to guide the eye. The vertical line and band show respectively the central value and the statistical error for the extrapolated β_c determined in Ref. [44].

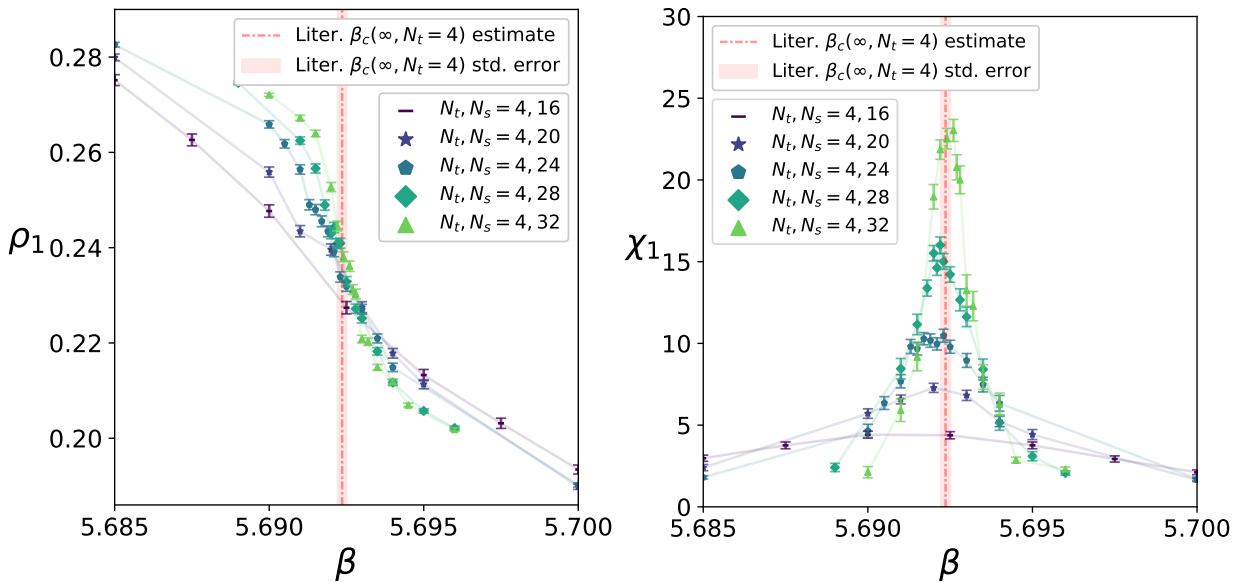


FIG. S3. For $N_t = 4$, a scatter plot of ρ_1 and χ_1 as functions of β with translucent lines to guide the eye. The vertical line and band show respectively the central value and the statistical error for the extrapolated β_c determined in Ref. [44].

Reweighting via density of states estimation

Our aim is to estimate the location of the peaks of χ_i ($i = 0, 1, \lambda$) so that we may extrapolate to the infinite volume limit $N_s \rightarrow \infty$. We use multiple histogram reweighting to extract a more precise location of the peak by estimating $\chi_i(\beta)$ at a high resolution of β -values covering the peak of our simulated values. This procedure involves learning the density of states of the system $\rho(E)$ where the partition function may be expressed

$$Z_\beta = \sum_E \rho(E) e^{-\beta E}. \quad (\text{S1})$$

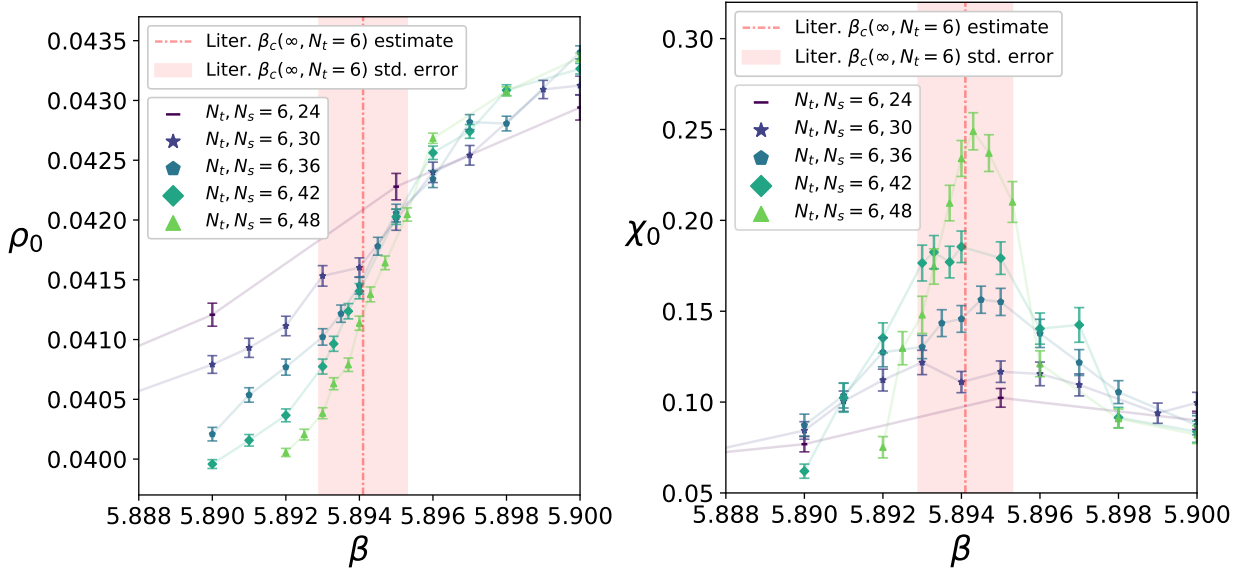


FIG. S4. For $N_t = 6$, a scatter plot of ρ_0 and χ_0 as functions of β zoomed into the critical region with translucent lines to guide the eye. The vertical line and band show respectively the central value and the statistical error for the extrapolated β_c determined in Ref. [44].

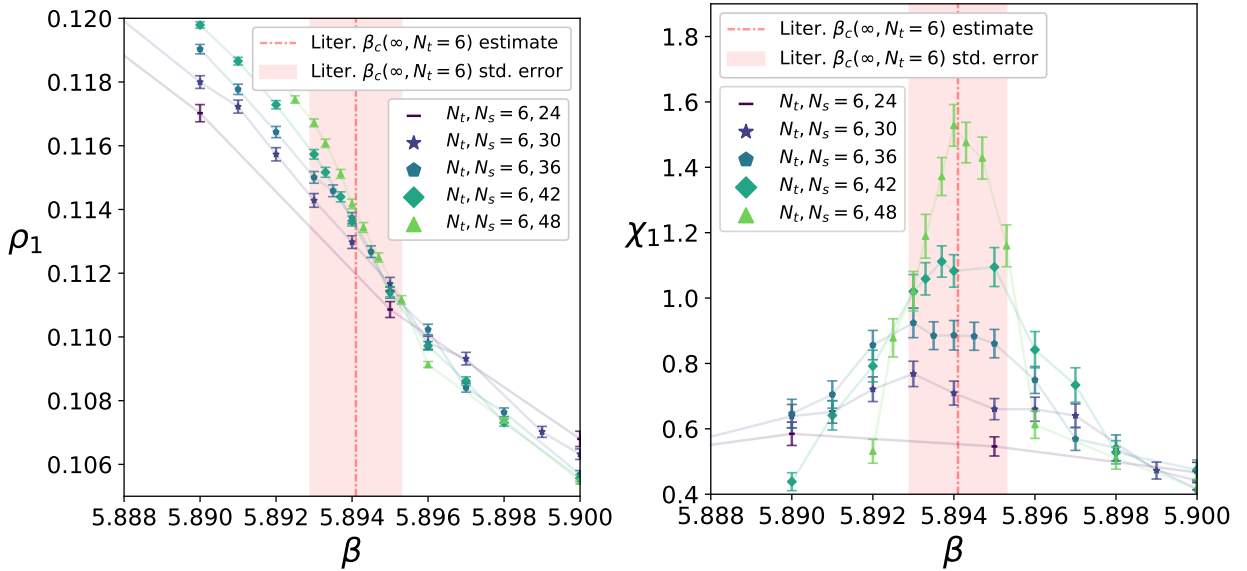


FIG. S5. For $N_t = 6$, a scatter plot of ρ_1 and χ_1 as functions of β zoomed into the critical region with translucent lines to guide the eye. The vertical line and band show respectively the central value and the statistical error for the extrapolated β_c determined in Ref. [44].

In practice, following Ref. [50], this is achieved implicitly by solving via iteration the equation

$$Z_\beta = \sum_{i=1}^R \sum_{a=1}^{N_i} \frac{g_i^{-1} e^{-\beta E_i^a}}{\sum_{j=1}^R N_j g_j^{-1} e^{-\beta_j E_i^a - \log Z_{\beta_j}}} \quad (S2)$$

where

- R is the number of simulations each respectively conducted at β_i with sample size N_i ,
- E_i^a is the energy measurement (in our case action) of the a -th recorded configuration in a simulation

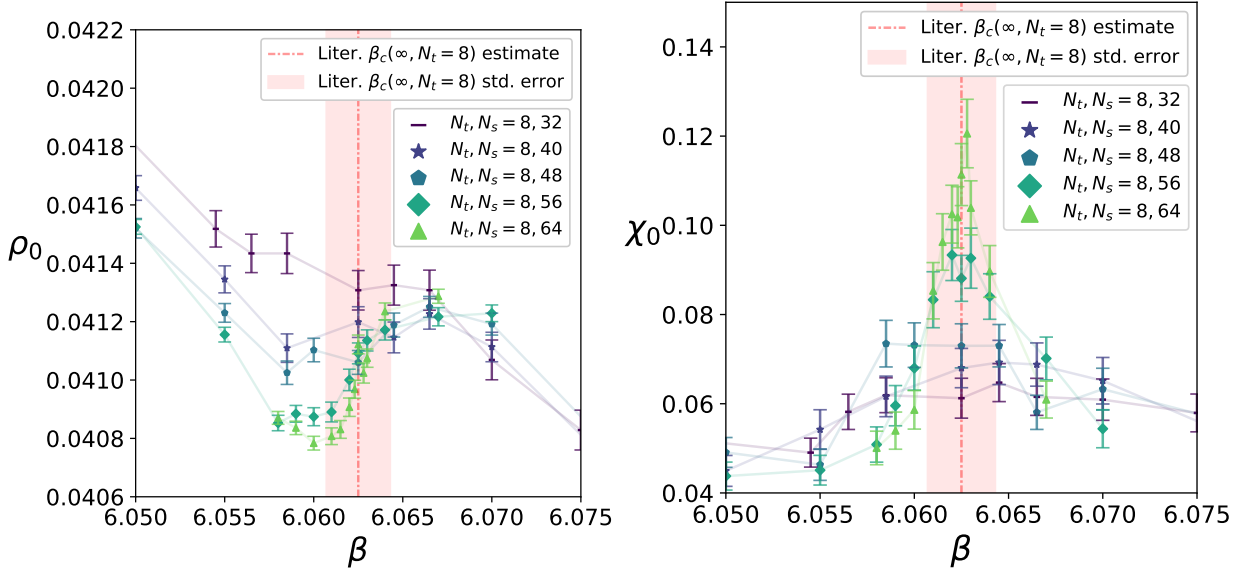


FIG. S6. For $N_t = 8$, a scatter plot of ρ_0 and χ_0 as functions of β zoomed into the critical region with translucent lines to guide the eye. The vertical line and band show respectively the central value and the statistical error for the extrapolated β_c determined in Ref. [44].

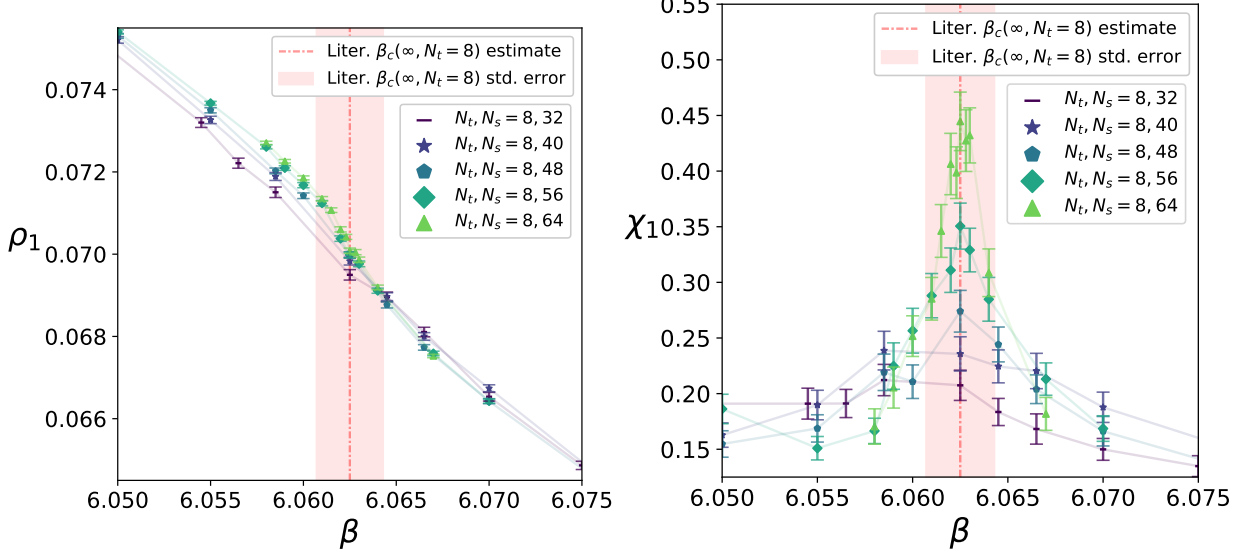


FIG. S7. For $N_t = 8$, a scatter plot of ρ_1 and χ_1 as functions of β zoomed into the critical region with translucent lines to guide the eye. The vertical line and band show respectively the central value and the statistical error for the extrapolated β_c determined in Ref. [44].

- and $g_i = 1 + 2\tau_i$ is a coefficient measuring the autocorrelation time between recorded configurations.

We may then estimate the expectation value of an observable O using

$$\langle O \rangle_\beta \approx \sum_{i=1}^R \sum_{a=1}^{N_i} \frac{O_i^a g_i^{-1} e^{-\beta E_i^a + \log Z_\beta}}{\sum_{j=1}^R N_j g_j^{-1} e^{-\beta_j E_j^a - \log Z_{\beta_j}}}. \quad (\text{S3})$$

Note that it can be a challenge to keep exponentials of the form $\exp\{-(\Delta\beta)S\}$ in a stable numerical range (avoiding underflow to 0) especially as the action S scales with lattice spacetime volume $N_t N_s^3$. Our algorithmic implementation in Ref. [46] uses long double precision and recentring to avoid numerical underflow.

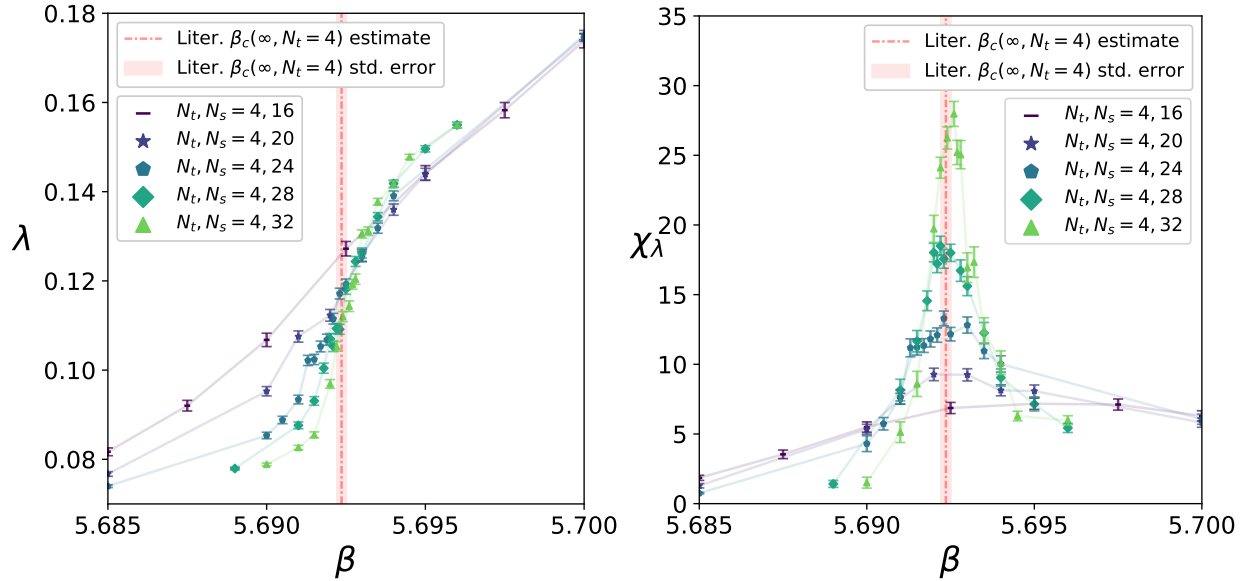


FIG. S8. For $N_t = 4$, a scatter plot of λ and χ_λ as functions of β with translucent lines to guide the eye. The vertical line and band show respectively the central value and the statistical error for the extrapolated β_c determined in Ref. [44].

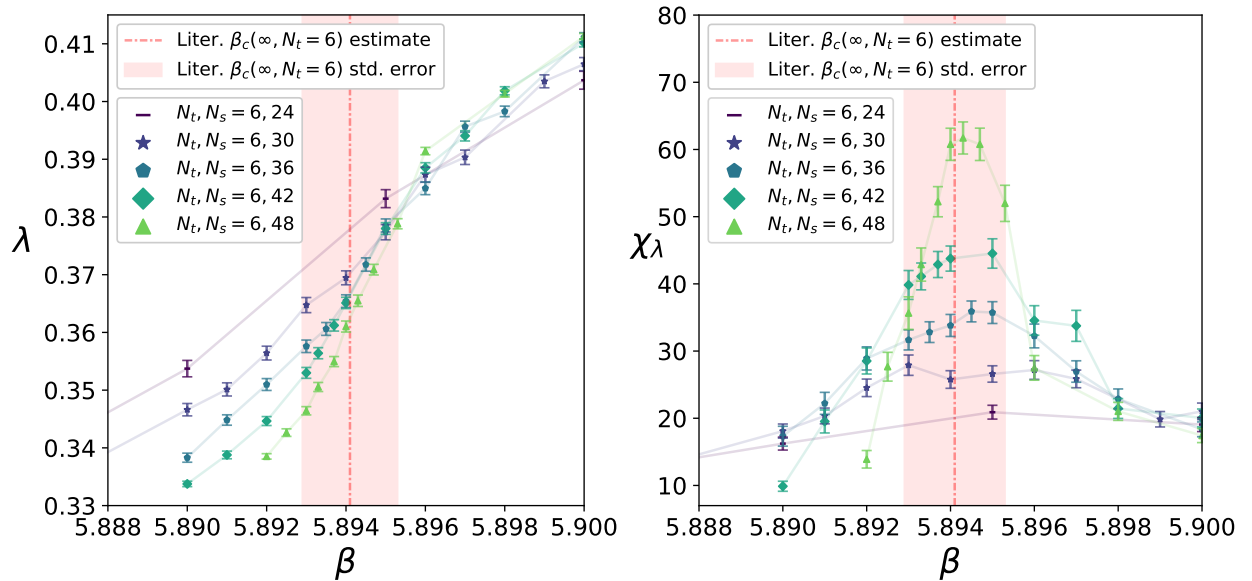


FIG. S9. For $N_t = 6$, a scatter plot of λ and χ_λ as functions of β with translucent lines to guide the eye. The vertical line and band show respectively the central value and the statistical error for the extrapolated β_c determined in Ref. [44].

In order to estimate the systematic error in the reweighting procedure, we use the bootstrap method with $N_{\text{bs}} = 2,000$. More specifically, following Ref. [50], given a simulation at β_i of sample size N_i , we estimate the autocorrelation τ_i between recorded configurations in the sample. Approximating $g_i \approx \tau_i$, we then randomly subsample to produce an effective sample of decorrelated configurations of size

$$N_i^{\text{eff}} = \lfloor N_i / \tau_i \rfloor, \quad (\text{S4})$$

where $\lfloor \cdot \rfloor$ is the floor function. To minimise autocorrelation, we use the RANLUX random number generator defined in Ref. [51]. Since configurations in this bootstrap sample are effectively decorrelated, this allows us to iteratively solve Eq. (S2) with $g_i = 1$. We take a convergence tolerance of 10^{-14} (smaller tolerances show compatible convergence). We thus have a resultant bootstrap distribution consisting of 2,000 reweighting curves.

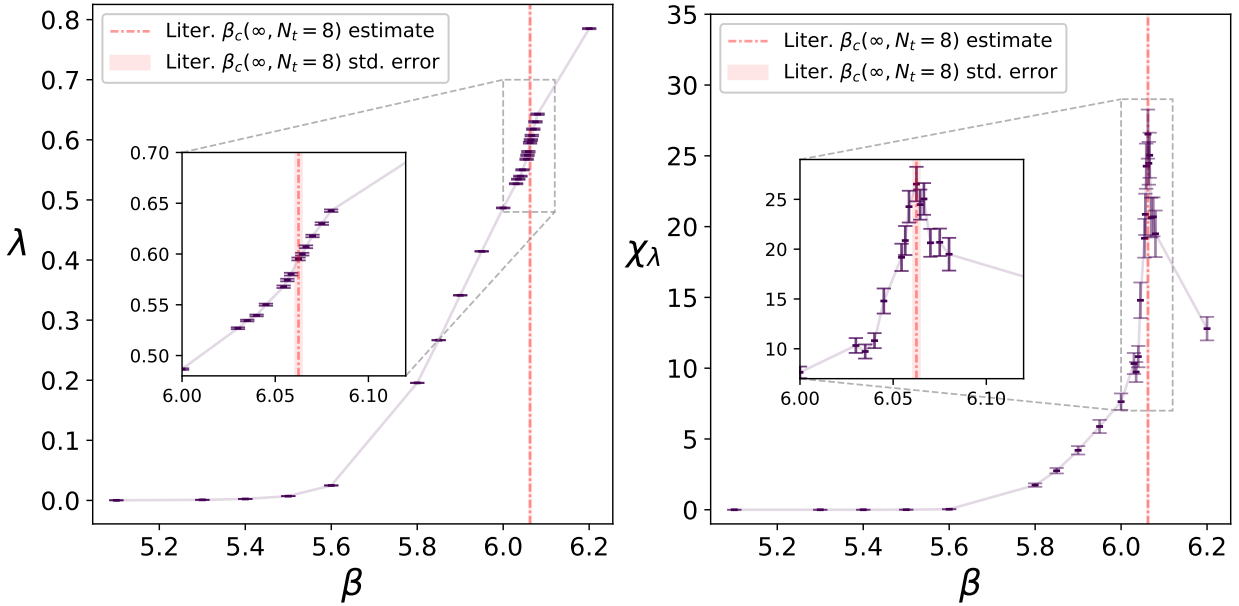


FIG. S10. For $N_t, N_s = 8, 32$, a scatter plot of λ and χ_λ as functions of β – with inset plot zoomed into the critical region. Translucent lines are included to guide the eye. One can see that $\lambda \in [0, 1]$ as expected. The red vertical line and band show respectively the central value and the statistical error for the extrapolated β_c determined in Ref. [44].

We extract $\beta_c = \text{argmax}\{\chi_i(\beta)\}$, the location of the peak of each curve, for every sample in the bootstrap distribution. We then take the mean as the estimate and standard deviation as the standard error.

Fitting of numerical results

In order to extrapolate the peaks of our observables $\beta_c(N_s, N_t)$, referred to as pseudo-critical values, to the thermodynamic limit $N_s \rightarrow \infty$, we fit the data using a polynomial ansatz in inverse powers of the spatial volume

$$\beta_c(N_s, N_t) = \beta_c(N_t) + \sum_{k=1}^{k_{\max}} \alpha_k (N_s^3)^{-k} \quad (\text{S5})$$

where $k_{\max} < \infty$ defines the degree of the polynomial. We perform a variety of fits varying the range of the data and polynomial degree. Note that we discard models with an extremal value within the range of datapoints since only subleading non-linear corrections are valid in the thermodynamic limit. The estimate for $\beta_c(N_t)$ is the intercept of each fit and we estimate the standard error again using the bootstrap method using $N_{\text{bs}} = 2,000$.

Rather than select an individual fit, we produce an estimate based on an ensemble of fits. Following Ref. [45], we use a statistic constructed from the Akaike Information Criterion (AIC) that considers goodness of fit, model complexity and degrees of freedom in the model. Roughly, the idea is to give strong weighting to models that have a high goodness of fit score, low model complexity and use all available data points. The normalised weights, interpreted as a probability, are calculated using the expression

$$w_i = \frac{1}{\mathcal{N}} \exp\left\{-\frac{1}{2}(\chi^2 + 2n_{\text{par}} - n_{\text{data}})\right\} \quad (\text{S6})$$

where χ^2 is the standard chi-squared statistic, n_{par} is the number of parameters in the model, n_{data} is the number of data points used in the fit and \mathcal{N} is the normalisation with respect to all fits. We then model the distribution by a weighted sum of Gaussian distributions with PDF

$$p(x) = \sum_i w_i N(x; \mu_i, \sigma_i) \quad (\text{S7})$$

with mean μ_i and standard deviation σ_i taken to be the statistical error in the estimate of the intercept (as estimated above via the bootstrap method). Taking the CDF of this distribution, we are able to solve numerically for the 16%,

Observable	$N_t = 4$	$N_t = 6$	$N_t = 8$
ρ_0	$5.69247^{+0.00005}_{-0.00006}$	$5.8942^{+0.0004}_{-0.0004}$	$6.0645^{+0.0014}_{-0.0017}$
ρ_1	$5.69257^{+0.00010}_{-0.00008}$	$5.8942^{+0.0006}_{-0.0004}$	$6.0625^{+0.0006}_{-0.0009}$
λ	$5.69240^{+0.00005}_{-0.00005}$	$5.8940^{+0.0004}_{-0.0004}$	$6.0625^{+0.0008}_{-0.0010}$
Literature value	$5.69236^{+0.00015}_{-0.00015}$	$5.8941^{+0.0012}_{-0.0012}$	$6.0625^{+0.0018}_{-0.0018}$

TABLE S1. Performing a finite-size scaling analysis using the Betti number observables, simplicity and their respective susceptibilities, this table specifies our estimates for β_c in the thermodynamic limit $N_s \rightarrow \infty$ for lattices with temporal size $N_t = 4, 6, 8$. Error bars are computed using the 68% confidence interval of the weighted sum of Gaussians encoding the various fits. As a comparison with the literature, the final row are results from Ref. [44]. This study used comparable MC methods to generate its configurations, which allows us to make a faithful comparison between the sensitivity (to the deconfinement phase transition) of our Abelian monopole observables with standard observables. In that study, the expectation value of the modulus of the average Polyakov loop $\langle |\bar{P}| \rangle$ was used such that the peaks of the respective susceptibilities $\chi_P(\beta)$ were used to give an estimate for β_c as $N_s \rightarrow \infty$. One can see that our results are compatible with those given in the literature.

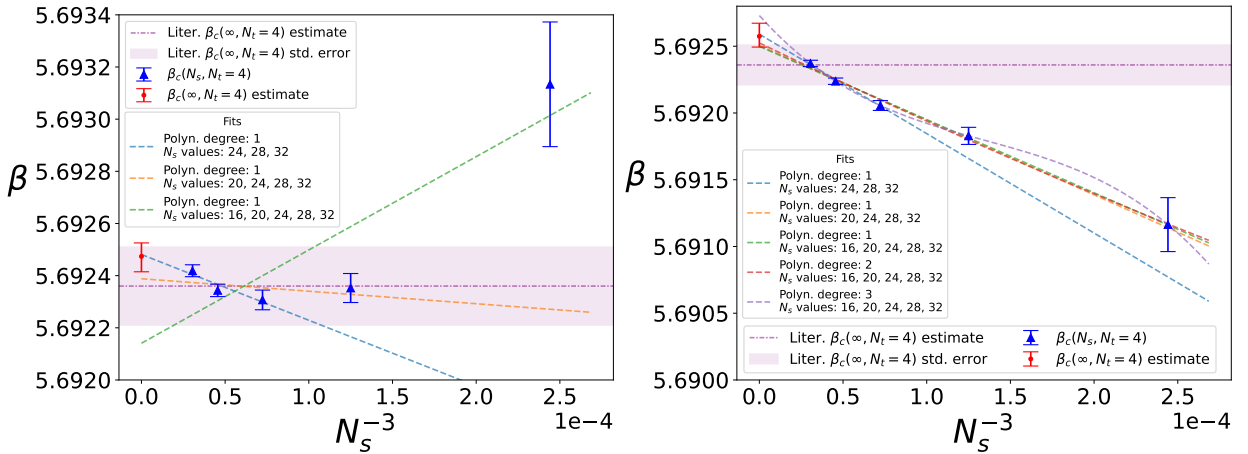


FIG. S11. Finite-size scaling analysis for the observables ρ_0 (left) and ρ_1 (right) both for lattices with $N_t = 4$ and $N_s = 16, 20, 24, 28, 32$. Blue triangles represent $\beta_c(N_s, N_t = 4)$, i.e., location of the respective peaks of the reweighted susceptibility curves, with error bars computed via bootstrapping with $N_{bs} = 2,000$. Dashed lines represent the polynomial regression fits used for the infinite volume extrapolation of these peak values. The red point is our calculated estimate of the β_c in the thermodynamic limit $N_s \rightarrow \infty$ using the weighting procedure outlined in the body. The horizontal line and band show respectively the central value and the statistical error for the extrapolated β_c determined in Ref. [44].

50%, 84% centiles as our lower bound, estimate and upper bound respectively. This final estimate represents weighted contributions from all fits and so we claim this is more robust than quoting estimates based on any single individual fit. Our estimates of β_c are presented in Tab. S1. Plots of scaling analysis for ρ_0 and ρ_1 are presented in Figs. S11, S12 and S13. Plots of scaling analysis for λ are presented in Figs. 2, 3 and 4.

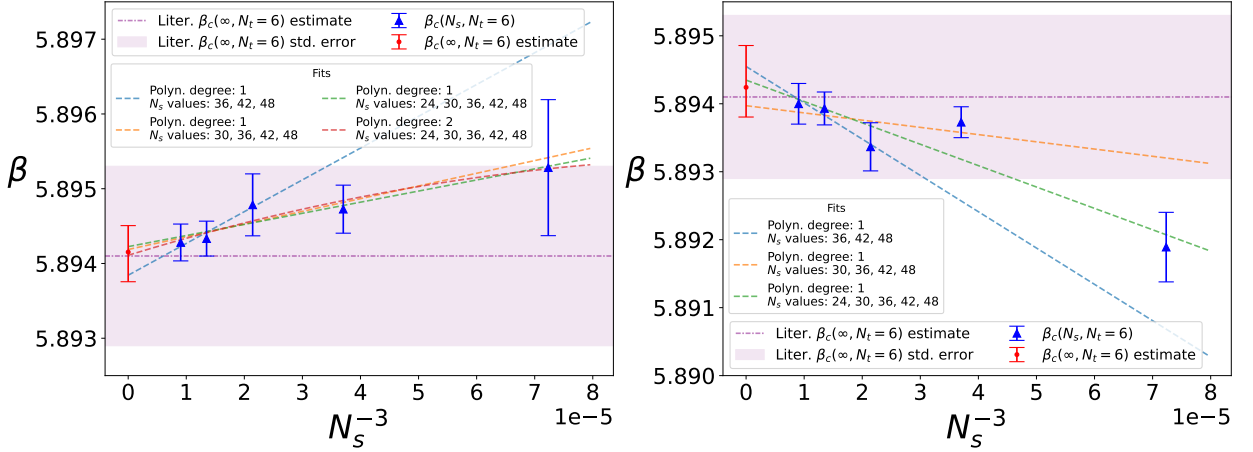


FIG. S12. Finite-size scaling analysis for the observables ρ_0 (left) and ρ_1 (right) both for lattices with $N_t = 6$ and $N_s = 24, 30, 36, 42, 48$. Blue triangles represent $\beta_c(N_s, N_t = 6)$, i.e., location of the respective peaks of the reweighted susceptibility curves, with error bars computed via bootstrapping with $N_{bs} = 2,000$. Dashed lines represent the polynomial regression fits used for the infinite volume extrapolation of these peak values. The red point is our calculated estimate of the β_c in the thermodynamic limit $N_s \rightarrow \infty$ using the weighting procedure outlined in the body. The horizontal line and band show respectively the central value and the statistical error for the extrapolated β_c determined in Ref. [44].

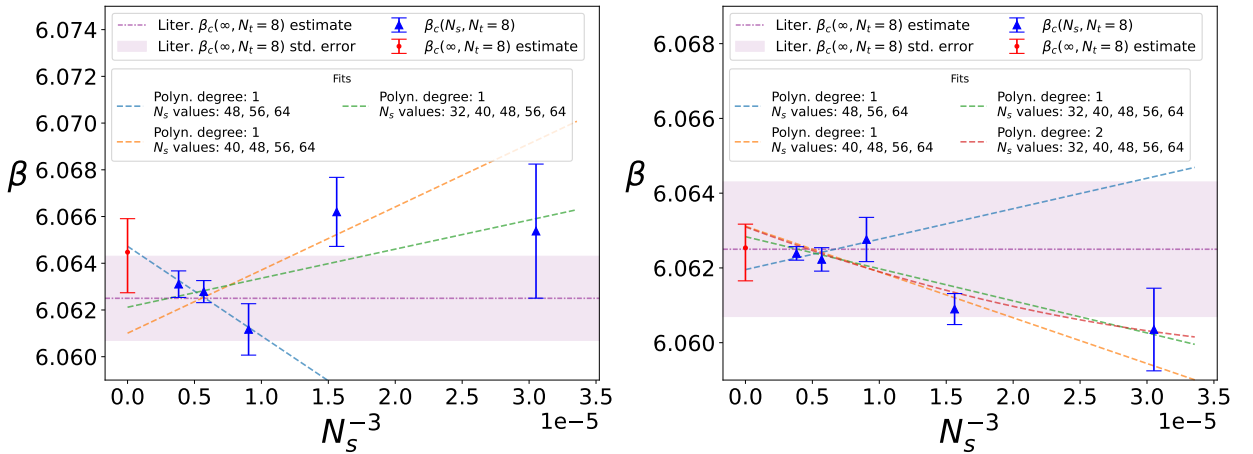


FIG. S13. Finite-size scaling analysis for the observables ρ_0 (left) and ρ_1 (right) both for lattices with $N_t = 8$ and $N_s = 32, 40, 48, 56, 64$. Blue triangles represent $\beta_c(N_s, N_t = 8)$, i.e., location of the respective peaks of the reweighted susceptibility curves, with error bars computed via bootstrapping with $N_{bs} = 2,000$. Dashed lines represent the polynomial regression fits used for the infinite volume extrapolation of these peak values. The red point is our calculated estimate of the β_c in the thermodynamic limit $N_s \rightarrow \infty$ using the weighting procedure outlined in the body. The horizontal line and band show respectively the central value and the statistical error for the extrapolated β_c determined in Ref. [44].